

Fast Multi-grid Methods for Minimizing Curvature Energies

Zhenwei Zhang, Ke Chen, and Yuping Duan*

Abstract—The geometric high-order regularization methods such as mean curvature and Gaussian curvature, have been intensively studied during the last decades due to their abilities in preserving geometric properties including image edges, corners, and image contrast. However, the dilemma between restoration quality and computational efficiency is an essential roadblock for high-order methods. In this paper, we propose fast multi-grid algorithms for minimizing both mean curvature and Gaussian curvature energy functionals without sacrificing the accuracy for efficiency. Unlike the existing approaches based on operator splitting and the Augmented Lagrangian method (ALM), no artificial parameters are introduced in our formulation, which guarantees the robustness of the proposed algorithm. Meanwhile, we adopt the domain decomposition method to promote parallel computing and use the fine-to-coarse structure to accelerate the convergence. Numerical experiments are presented on both image denoising and CT reconstruction problem to demonstrate the ability to recover image texture and the efficiency of the proposed method.

Index Terms—Mean curvature, Gaussian curvature, multi-grid method, domain decomposition method, image denoising, CT reconstruction.

I. INTRODUCTION

CURVATURE regularization is well-known for its good geometric interpretability and strong priors in the continuity of edges, which has been applied to various data processing tasks such as image decomposition [1], graph embedding [2], and missing data recovery [3] etc.

Image restoration aims to recover the latent clean image u from the observed noisy image $f : \Omega \rightarrow \mathbb{R}$ defined on an open bounded domain $\Omega \subset \mathbb{R}^2$. The total variation (TV) proposed by Rudin, Osher, Fatemi is the most successful regularization used for image denoising problem [4], which minimizes the total lengths of all level sets of the image. Although the ROF model has been proven to effectively remove noise and preserve sharp edges, it also suffers from some unfavorable properties including loss of image contrast and staircase effect [5]. High-order regularization methods have been investigated for image restoration problem to overcome the drawback of TV regularization including the fourth-order partial differential equation (PDE) [6], total generalized variation [7], Euler's Elastica [8], mean curvature [9] and total roto-translational

The work was partially supported by the National Natural Science Foundation of China (NSFC 12071345, 11701418), Major Science and Technology Project of Tianjin 18ZXHHSY00160, and Recruitment Program of Global Young Expert. Asterisk indicates the corresponding author.

Z. Zhang and Y. Duan are with Center for Applied Mathematics, Tianjin University, Tianjin 300072, China. E-mail: yuping.duan@tju.edu.cn.

K. Chen is with Department of Mathematical Sciences, University of Liverpool, United Kingdom.

variation [10] etc. Among them, the curvature regularization methods achieved great success by minimizing curvature-dependent energies. Considering the associated image surface characterized by $(x, f(x))$ for $x \in \Omega$, the image restoration problem becomes to find a piecewise smooth surface $(x, u(x))$ to approximate the noisy surface and simultaneously remove the outliers. The corresponding curvature minimization problem can be formally formulated as follows

$$\min_u \int_{\Omega} |\kappa(u)| dx + \frac{\alpha}{2} \int_{\Omega} (u - f)^2 dx, \quad (1)$$

where $\kappa(u)$ can be either mean curvature or Gaussian curvature of the image surface. Compared to the previous type, the minimization of curvatures is more challenging, such that efficient algorithms for solving the model (1) are still limited. Originally, the gradient descent method [9] was presented to solve mean curvature model, which has to solve fourth-order nonlinear evolution equations. Zhu, Tai and Chan [11] developed the augmented Lagrangian method (ALM) for the mean curvature model. Brito-Loeza and Chen [12] propose a multi-grid algorithm for solving the mean curvature model, which is based on an augmented Lagrangian formulation with a special linearized fixed point iteration. The situation is even worse for Gaussian curvature minimization since no fast algorithms are developed yet. There are not many studies of effective numerical algorithms for Gaussian curvature minimization. Alboul and van Damme [13] used the total absolute Gaussian curvature in the different contexts of connectivity optimization for the triangulated surfaces. Elsey and Esedoglu [14] introduced the Gaussian curvature regularization for surface processing as the natural analog of the total variation, which is discretized on a triangulated surface for reducing the difficulty of solution. Brito-Loeza and Chen [15] presented a two-step method based on vector field smoothing and gray level interpolation, then only two second-order equations need to be solved.

Zhong, Yin and Duan [16] formulated the following curvature regularization model by minimizing either Gaussian curvature or mean curvature over image surfaces

$$\min_u \int_{\Omega} g(\kappa) \sqrt{1 + |\nabla u|^2} dx + \frac{\lambda}{2} \int_{\Omega} (u - f)^2 dx, \quad (2)$$

where $g(\cdot)$ denotes a certain function of the curvature. Model (2) was regarded as a re-weighted minimal surface model and handled by the alternating direction method of multipliers (ADMM). Although the curvature function can be explicitly evaluated using the current estimation, one nonlinear sub-minimization problem has to be computed by Newton method resulting in the rising computational costs.

Gong and Sbalzarini [17] developed the curvature filters by minimizing either Gaussian curvature or mean curvature to smooth the noisy images. Rather than solving the higher order PDEs, the pixel-wise solutions were presented to find the locally developable and minimal surfaces, which give the zero Gaussian curvature and zero mean curvature, respectively. However, the curvatures lack rigorously definition, which limit its performance on real applications. Besides, when combined with the data fidelity term, gradient descent was used to estimate the solution leading to the slow convergence.

The multi-grid method is a fast numerical method for solving large-scale linear and nonlinear optimization problems [18]–[21], and has been successfully applied to image processing models. Chen and Tai [22] proposed a nonlinear multi-grid method for the total variation minimization based on the coordinate descent method. Savage and Chen [23] presented a nonlinear multi-grid method based on the full approximation scheme for solving the total variation model. Chan and Chen [24] proposed a fast multilevel method using primal relaxations for the total variation image denoising and analyzed its convergence. Zhang *et al.* [25] developed a multi-level domain decomposition method for solving the total variation minimization problems, which used the piecewise constant functions spanned subspace correction to ensure fast computation. Tai, Deng and Yin [26] proposed a multiphase image segmentation method via solving the min-cut minimization problem under the multi-grid method framework. For the high-order model, Brito-Loeza and Chen [12] presented a new multi-grid method based upon a stabilized fixed point method for dealing with the mean curvature model. The nonlinear multi-grid method was applied to fourth-order models to accelerate the convergence in [27]. However, these methods require very high computational costs to solve the high-order PDEs and result in low efficiency.

This work is to present the efficient multi-grid method for solving the highly nonlinear curvature regularization models. We formulate a patch-based correction strategy from the fine grid layer to coarse grid layers and then interpolate the correction to each point nodal belonging to the patch. We proposed a forward-backward splitting scheme [28], [29] to solve the curvature minimization problem, and proves its convergence theoretically. More specifically, we first obtain analytical solutions to the mean curvature/Gaussian curvature minimization based on the local geometry property. In what follows, we solve a convex optimization problem to estimate the patch-wise update. To further improve the efficiency, we use the four-color domain decomposition method on each layer to enable all subproblems in the same color to be solved in parallel. Numerous numerical experiments on both image restoration and CT reconstruction are presented to demonstrate the efficiency and effectiveness of our algorithm in dealing with large-scale image processing problems. To sum up, our contributions are concluded as follows

- We develop an efficient multi-grid method for solving the curvature minimization problem (1) using the piecewise constant function spanned subspace correction, where the minimization over the whole space is transferred into small-size local patches;

- We use the forward-backward splitting scheme to solve the non-convex patch-wise minimization problem, where both subproblems can be efficiently handled by the closed-form solutions;
- The non-overlapping domain decomposition method is applied to circumvent the dependencies between the adjacent patches, which enables the parallel computation from the fine layer to the coarse layers;
- The application of the mean curvature minimization is extended to CT reconstruction problems to prove our approach can well balance the image quality and computational efficiency.

The rest of the paper is organized as follows. In Sect. II, the coordinate descent methods are proposed to solve mean curvature minimization problem and the coarse grid structure is used to relax the problem. We extend the idea to Gaussian curvature minimization in Sect. III. Numerical experiments are conducted to illustrate the advantages by comparing with curvature filters and other curvature-related models in Sect. IV. In Sect. V, the multi-grid algorithm is extended to solve image reconstruction problem. We conclude the paper in Sect. VI with some remarks and future works.

II. THE MEAN CURVATURE MINIMIZATION PROBLEM

Assume that the gray scale image domain Ω is composed of $m \times n$ pixels. Letting $H(u)$ be the mean curvature, we concern with the following discrete mean curvature energy

$$\min_{u \in V} F(u) := \sum_{(k_1, k_2) \in \Omega} \left\{ |H(u_{k_1, k_2})| + \frac{\alpha}{2} (u_{k_1, k_2} - f_{k_1, k_2})^2 \right\}, \quad (3)$$

where V is a function space that needs to be chosen carefully. To the best of our knowledge, one has not identified the proper function to formulate problem (3), which should be a subset of $L^2(\Omega)$.

Our task is to find a surface to fit the original image surface and compel the mean curvature as small as possible. Instead of solving the high-order PDEs, we follow the multi-grid method to interpret the minimization problem (3) as estimating the best correction to the current approximation. More precisely, we solve the minimization (3) by finding the optimal correction over each pixel $(k_1, k_2) \in \Omega$ as follows

$$\min_{c \in \mathbb{R}} J(c) := |H(u_{k_1, k_2} + c)| + \frac{\alpha}{2} (c - f_{k_1, k_2}^*)^2, \quad (4)$$

where $c \in \mathbb{R}$ denotes the pixel-wise correction and $f_{k_1, k_2}^* = f_{k_1, k_2} - u_{k_1, k_2}$. As can be seen, the original minimization problem (3) is transferred into the one-dimensional minimization problem, and the core issue becomes how to solve (4) effectively.

We use the forward-backward splitting (FBS) method to reformulate the local problem (4) into a couple of sub-minimization problems. The forward-backward algorithm is a popular choice for sparse regularization with a smooth data fidelity, see for instance [30], [31]. Although our minimization is non-convex, we can theoretically prove the convergence of the proposed FBS algorithm. The detailed algorithm is described as Algorithm 1.

Algorithm 1: The forward-backward splitting method for solving the local minimization problem (4)

1. Input $u_{k_1, k_2} = 0$, and $\alpha > 0$, $\eta^0 = 1$;
2. For each $t = 0, 1, 2, \dots$ compute u_{k_1, k_2}^{t+1} by solving

$$\left\{ \begin{array}{l} c^{t+\frac{1}{2}} = \arg \min_c |H(u_{k_1, k_2}^t + c)|; \\ c^{t+1} = \arg \min_c \frac{1}{2}(c - c^t - (\eta^t)^2 c^{t+\frac{1}{2}})^2 + \frac{\alpha \eta^t}{2} (c - f_{k_1, k_2}^*)^2; \end{array} \right. \quad (5)$$

$$\left\{ \begin{array}{l} u_{k_1, k_2}^{t+1} = u_{k_1, k_2}^t + c^{t+1}; \\ \eta^{t+1} = \frac{1}{\sqrt{1+t}}; \end{array} \right. \quad (6)$$

3. End till some stopping criterion meets.

Solution to sub-minimization (5). We can use the geometric interpretation to estimate the correction in a local window according to the well-known Bernstein's theorem.

Proposition 1. Let d_ℓ denote the distances of (k_1, k_2, u_{k_1, k_2}) on the image surface leaving from the tangent planes and ι be the total number of tangent planes. The mean curvature energy $|H(u_{k_1, k_2} + c)|$ decreases when the correction c is defined as $c = \frac{1}{\iota} \sum_{\ell=1}^{\iota} d_\ell$.

Proof. According to Bernstein's theorem, a graph of a real function on \mathbb{R}^2 is a minimal surface in \mathbb{R}^3 must be a plane. Thus, the flatter the image surface, the smaller the mean curvature regularization term. Suppose there are ι tangent planes and the corresponding distances of (k_1, k_2, u_{k_1, k_2}) to its tangent planes are denoted by d_ℓ , $\ell = 1, \dots, \iota$. To make the image surface as flat as possible, we consider the following quadratic minimization problem

$$\min_{c \in \mathbb{R}} \sum_{\ell=1}^{\iota} (c - d_\ell)^2,$$

where the optimal correction is $c = \frac{1}{\iota} \sum_{\ell=1}^{\iota} d_\ell$. \square

Consequently, we enumerate the local tangent planes in a 3×3 window. As shown in Fig. 1, there are all eight tangent planes in the local window, where the tangent planes T_1 to T_8 are pairwise centrosymmetric to avoid the grid bias. Similar to our previous work [16], we compute the distances d_ℓ , $\ell = 1, \dots, 8$, as illustrated in Fig. 2. Let the plane XYZ be a tangent plane of O and \mathbf{n} denote the normal vector. The directed distance from O to the tangent plane can be calculated by $d = \overrightarrow{XO} \cdot \mathbf{n}$, where \mathbf{n} is defined by the cross product of the vector \overrightarrow{XZ} and \overrightarrow{XY} , i.e., $\mathbf{n} = \overrightarrow{XZ} \times \overrightarrow{XY}$. Then, we have

$$d = \overrightarrow{XO} \cdot \mathbf{n} =$$

$$\frac{(u_{k_1, k_2-1} + u_{k_1, k_2+1} - 2u_{k_1, k_2})}{\sqrt{(u_{k_1, k_2-1} + u_{k_1, k_2+1} - 2u_{k_1-1, k_2})^2 + (u_{k_1, k_2+1} - u_{k_1, k_2-1})^2 + 4}}.$$

The computation of d_ℓ , $\ell = 1, \dots, 8$, can be implemented in the same way. And the update of $c^{t+\frac{1}{2}}$ can be estimated as

$$c^{t+\frac{1}{2}} = \frac{1}{8} \sum_{\ell=1}^8 d_\ell. \quad (9)$$

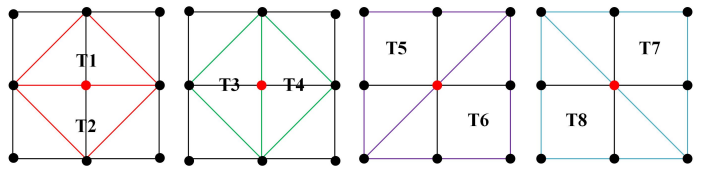


Fig. 1. Illustration of the eight tangent planes located in a 3×3 local patch on the finest layer, which locate pairwise centrosymmetric concering the center point nodal (marked by red color).

Solution to sub-minimization (6). We are facing a quadratic minimization problem, which has the closed-form solution as

$$c^{t+1} = \frac{1}{1 + 2\alpha\eta^t} \left(c^t + \alpha\eta^t f^* + (\eta^t)^2 c^{t+\frac{1}{2}} \right). \quad (10)$$

A. Convergence analysis of Algorithm 1

In the subsection, we present a brief convergence analysis of Algorithm 1. Due to the energy decay property obtained by Proposition 1, our algorithm can fall into the algorithmic framework of the forward-backward splitting scheme in [32]. Let c^* denote the minimizer of model (4) and the date fidelity term be denoted by $r(c) = \frac{\alpha}{2}(c - f_{k_1, k_2}^*)^2$. The next lemma provides a key tool for deriving convergence.

Lemma 1. (Bounding Step Differences) We assume that the gradient of $r(c)$ is bounded by a constant G as follows

$$\|\nabla r(c)\|^2 \leq G.$$

Suppose $c^{t+\frac{1}{2}}$ is a minimizer of (5), then for any constant \tilde{c} less than D , we have

$$2\eta^t (|H(u^t + c^{t+\frac{1}{2}})| + r(c^{t+1}) - J(\tilde{c})) \leq \|c^t - \tilde{c}\|^2 - \|c^{t+1} - \tilde{c}\|^2 + 2(\eta^t)^2 (G + D).$$

Proof. The proof is sketched in Appendix. \square

Based on Lemma 1, we can prove the following result, which is the basis for deriving convergence results.

Lemma 2. Assume that the norm of $c^{t+\frac{1}{2}}$, we sum the residuals over t from 1 through T and get a telescoping sum:

$$\sum_{t=1}^T \eta^t \left[|H(u^t + c^{t+\frac{1}{2}})| + r(c^{t+1}) - J(\tilde{c}) \right] \leq \tilde{G},$$

where $\tilde{G} = \sum_{t=1}^T 2(\eta^t)^2 (G + D) + D$.

Proof. The proof is similar to Theorem 2 in [32]. \square

Therefore, a direct consequence of Lemma 2 is the convergence when running Fobos with $\eta^t \propto 1/\sqrt{t}$ or with non-summable step sizes decreasing to zero.

Theorem 1. Assume that the step size η^t satisfy $\eta^t \rightarrow 0$, $\sum_{t=1}^{\infty} \eta^t = \infty$ and $\sum_{t=1}^{\infty} (\eta^t)^2 \leq \infty$. Then we have

$$\lim_{t \rightarrow \infty} J(c^t) - J(c^*) = 0. \quad (11)$$

Proof. It is clear that $c^{t+\frac{1}{2}} = c^{t+1}$ when $t \rightarrow \infty$. For T iterations, the bound of convergence rate from Lemma 2 becomes

$$(J(c^T) - J(\tilde{c})) \sum_{t=1}^T \eta^t \leq \sum_{t=1}^T \eta^t \left[|H(u^t + c^{t+\frac{1}{2}})| + r(c^{t+1}) - J(\tilde{c}) \right].$$

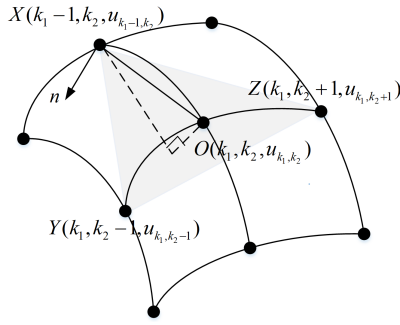


Fig. 2. Illustration of the distance to the tangent plane, where $x = (k_1, k_2)$ indicates the coordinates and u denotes the image intensity function.

Therefore, let $\tilde{c} = c^*$, we have

$$\lim_{t \rightarrow \infty} J(c^t) - J(c^*) \leq \frac{\tilde{G}}{\sum_{t=1}^{\infty} \eta^t} \rightarrow 0.$$

Then it holds $\lim_{t \rightarrow \infty} J(c^t) - J(c^*) = 0$. \square

Remark 1. The step size η can be a constant or diminishing with iterations. We let $\eta^t = 1/\sqrt{t}$ in numerical experiments.

B. Our multi-grid algorithm

Regarding problem (4) as the finest grid, we can use a larger local window with current approximate u and generate the multi-grid algorithm for (3). Without loss of generality, we assume the initial grid \mathcal{T} consists of $m \times n$ grid points. Starting from finest grid $\mathcal{T}_1 = \mathcal{T}$, we consider a sequence of coarse structure, $\mathcal{T}_1, \mathcal{T}_2, \dots, \mathcal{T}_J$, with J being the total number of layers. Our multi-grid structure is constructed by gathering the grids point into non-overlapping patches of different sizes. Specifically, the size of the patch set τ_j on the j th coarse layer is $(2^j - 1) \times (2^j - 1)$, and \mathcal{T}_j contains $m_j \times n_j$ patches with

$$m_j = \lceil m/(2^j - 1) \rceil, \quad n_j = \lceil n/(2^j - 1) \rceil,$$

where $\lceil \cdot \rceil$ is a rounding up function. Then there are $N_j = m_j \times n_j$ patches on the j th coarse layers and the partition can be expressed as $\mathcal{T}_j = \{\tau_j^i\}_{i=1}^{N_j}$. In order to ensure each patch is complete, we prolongate the image domain before the partition using boundary conditions. It is straightforward to define V_j as a finite element space

$$V_j = \{v : v|_{\tau_j} \in \mathcal{P}_c(\tau_j), \forall \tau_j \in \mathcal{T}_j\},$$

where \mathcal{P}_c denotes the space of all piecewise constant functions. We equip the piecewise constant function space V_j with a set of basis functions $\{\phi_j^i\}_{i=1}^{N_j}$, which is defined as

$$\phi_j^i(x) = \begin{cases} 1, & \text{if } x \in \tau_j^i; \\ 0, & \text{if } x \notin \tau_j^i; \end{cases} \quad i = 1, \dots, N_j. \quad (12)$$

Associated with each basis function, we define the one dimensional subspace $V_j^i = \text{span}\{\phi_j^i\}$. Then, the whole space V can be expressed as $V = \sum_{j=1}^J \sum_{i=1}^{N_j} V_j^i$.

On the coarse grids, we consider a larger local patch including more local tangent planes to be enumerated. We can come up with a recurrence formula for the number of tangent planes on the j th layer as $\iota = 2^{j+2}$. For example, we

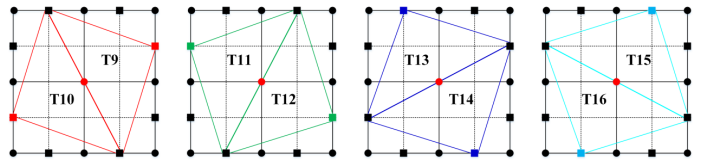


Fig. 3. Illustration of the eight tangent planes $T_9 - T_{16}$ together with $T_1 - T_8$ in Fig. 1 form a coherent whole for a 5×5 patch on the first coarse layer.

enumerate the total of 16 triangular planes for patches on the first coarse layer, half of which are the same as the finest layer and the left ones are displayed in Fig. 3. When implementing Algorithm 1 to solve the local minimization problem, we use all distances defined on the local patch. Correspondingly, the sequence of one-dimensional subspace minimization problems over the subspace V_j^i is given below

$$\min_{c^{t+1} \in \mathbb{R}} \frac{1}{2} (c^{t+1} - c^t - (\eta^t)^2 \frac{1}{16} \sum_{\ell=1}^{\iota} d_{\ell})^2 + \frac{\eta^t \alpha s}{2} (c^{t+1} - f^*)^2, \quad (13)$$

for $i = 1, \dots, N_j$, $j = 1, \dots, J$, where $f^* = \sum_{x \in \tau_j^i} (f(x) - u^t(x))/s$ and $s = \sum_{x \in \tau_j^i} \phi_j^i(x)$. And the closed-form solution is defined as follows

$$c^{t+1} = \frac{1}{1 + \eta^t \alpha s} \left(c^t + (\eta^t)^2 \frac{1}{16} \sum_{\ell=1}^{\iota} d_{\ell} + \eta^t \alpha s f^* \right).$$

In particular, we can obtain the following matrix of size $m_j \times n_j$ on the j th layer after the computation on each local patch

$$c^{(j)} = \begin{bmatrix} \dots & \vdots & \vdots & \vdots & \dots \\ \vdots & c_{t_1-1, t_2-1}^{(j)} & c_{t_1-1, t_2}^{(j)} & c_{t_1-1, t_2+1}^{(j)} & \vdots \\ \vdots & c_{t_1, t_2-1}^{(j)} & c_{t_1, t_2}^{(j)} & c_{t_1, t_2+1}^{(j)} & \vdots \\ \vdots & c_{t_1+1, t_2-1}^{(j)} & c_{t_1+1, t_2}^{(j)} & c_{t_1+1, t_2+1}^{(j)} & \vdots \\ \dots & \vdots & \vdots & \vdots & \dots \end{bmatrix}_{m_j \times n_j},$$

where m_j and n_j denote the number of patches on row direction and column direction, respectively. Because we use the piecewise constant basis function over the support set, we can define an interpolation matrix $L_j : \mathbb{R}^{m_j n_j} \rightarrow \mathbb{R}^{mn}$ used to update the solution on the finest layer, i.e.

$$L_j c^{(j)} = \begin{bmatrix} \vdots & \vdots & \vdots & \vdots & \vdots \\ c_{t_1-1, t_2-1}^{(j)} & c_{t_1-1, t_2}^{(j)} & \dots & c_{t_1-1, t_2}^{(j)} & c_{t_1-1, t_2+1}^{(j)} \\ c_{t_1, t_2-1}^{(j)} & c_{t_1, t_2}^{(j)} & \dots & c_{t_1, t_2}^{(j)} & c_{t_1, t_2+1}^{(j)} \\ \dots & \vdots & \dots & \vdots & \dots \\ c_{t_1, t_2-1}^{(j)} & c_{t_1, t_2}^{(j)} & \dots & c_{t_1, t_2}^{(j)} & c_{t_1, t_2+1}^{(j)} \\ c_{t_1+1, t_2-1}^{(j)} & c_{t_1+1, t_2}^{(j)} & \dots & c_{t_1+1, t_2}^{(j)} & c_{t_1+1, t_2+1}^{(j)} \\ \vdots & \vdots & \dots & \vdots & \vdots \end{bmatrix}_{m \times n}$$

Then the solution can be defined as $u^{t+1} = u^t + L_j c^{(j)}$.

We use the V-cycle to solve the minimization model from the finest layer V_1 to the coarsest layer V_J , and then from the coarsest layer to the finest layer. In practice, we find that half of the V-cycle is sufficient for the decrease of the energy functional, while the other half of the V-cycle does

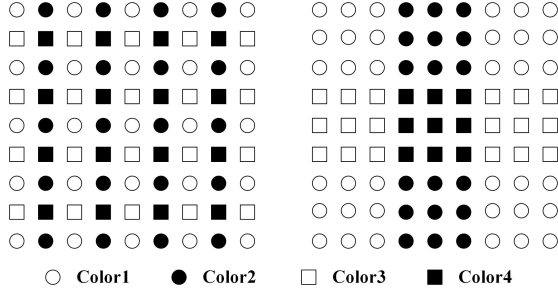


Fig. 4. Illustration of 4-color domain decomposition for a domain of size 9×9 , where the subproblems of the same color can be computed in parallel.

little improvement. Thus the coarse to fine subspace correction can be omitted.

C. The domain decomposition strategy

The domain decomposition method (DDM) is another promising technique to deal with large-scale problems, which divides the large-scale problem into smaller problems for parallel computation. In the following, we will apply the non-overlapping domain decomposition method to enable parallel computation.

Fig. 4 displays the four-color decomposition on the finest layer and the second layer, respectively. More specifically, we divide the basis function $\{\phi_j^i\}_{i=1}^{N_j}$ into four groups $\bigcup_{k=1}^4 \{\phi_j^i : i \in I_k\}$ to reduce the dependency on the order of basis functions and improve the parallelism for subproblems on each layer, where I_k contains the indexes with the same color. This decomposition guarantees that neighboring patches in a 4-connected neighborhood are in different subsets. We can see that the support of the basic functions $\{\phi_j^i : i \in I_k\}$ are non-overlapping for each $k = 1, 2, 3, 4$, and the minimization of $F(u + c\phi_j^i)$ for $i \in I_k$ can be solved in parallel. In particular, four subproblems are solved in consecutive order

$$\min_{\delta u \in V_j^{(k)}} F(u + \delta u), \quad \text{for } k = 1, 2, 3, 4,$$

where $V_j^{(k)} = \text{span}\{\phi_j^i : i \in I_k\}$ and $V_j = \sum_{k=1}^4 V_j^{(k)}$. It is readily checked that

$$\min_{\delta u \in V_j^{(k)}} F(u + \delta u) = \min_{\mathbf{c} \in \mathbb{R}^{|I_k|}} F(u + \sum_{i \in I_k} c_j^i \phi_j^i), \quad (14)$$

where $\mathbf{c} = (c_j^1, c_j^2, \dots, c_j^{|I_k|})$ with $|I_k|$ being the total number of elements in I_k and $N_j = \sum_{k=1}^4 |I_k|$.

Then, the implementation of the algorithm to solve the mean curvature minimization problem (3) is summarized in Algorithm 2.

D. Complexity analysis

In this section, the floating point operations (FLO) is used to evaluate the complexity of the algorithm. The cost of our method is mainly related to the following two parts. The first is the distances to the tangent planes d_ℓ , which is about $4 \times 2^{j+2}$ floating point operations (FLO) on each patch set τ_j^i . Therefore, the total cost on the coarse level j is about $\mathcal{O}(4m_j n_j 2^{j+2}) \approx \mathcal{O}(4mn/(2^j - 1))$. The second cost is

Algorithm 2: The multi-grid method for solving the mean curvature minimization model

Input: $f, u^0, \alpha, \epsilon, N_t$;
for $t = 1$ to T /* Outer iterations */
do
 for $j = 1$ to J /* From the fine layer to coarse layer */
 do
 for $k = 1$ to 4, /* the four-color DDM iterations */
 do
 $\mathbf{c} = \arg \min_{\mathbf{c} \in \mathbb{R}^{|I_k|}} F(u + \sum_{i \in I_k} c_j^i \phi_j^i);$
 $u^{t+j+\frac{k}{4}} \leftarrow u^{t+j+\frac{k-1}{4}} + \sum_{i \in I_k} c_j^i \phi_j^i.$
 end
 end
 end
 end
end
Output: u .

the interpolation operator L_j , which is about mn FLO. The computation of f^* is about $2(2^j - 1)(2^j - 1)m_j n_j \approx 2mn$. Then the number of FLOs over all J levels should be $\mathcal{O}(\sum_{j=1}^J (3 + 4/(2^j - 1))mn)$. In particular, the computational complexity of our multi-grid algorithm with 3 layers is about $\mathcal{O}(12mn)$.

As a point of reference, the mean curvature method [11] contains three sub-problems, which can be solved by either the shrinkage operation or the FFT with the total computational complexity of $\mathcal{O}(6mn \log mn + 8mn)$. The computational complexity of the total absolute mean curvature model [16] and Euler's elastica model [8] can be obtained similarly, which are $\mathcal{O}(2mn \log mn + 3mn)$ and $\mathcal{O}(6mn \log mn + 4mn)$, respectively. It is shown that our multi-grid algorithm is with much low computational complexity compared to the existing high order methods.

III. THE GAUSSIAN CURVATURE MINIMIZATION PROBLEM

We can directly extend the proposed multi-grid method to solve the following Gaussian curvature minimization problem

$$\min_{u \in V} \alpha \sum_{x \in \Omega} |K(u(x))| + \frac{1}{2} \sum_{x \in \Omega} (u(x) - f(x))^2, \quad (15)$$

where $K(u)$ is the Gaussian curvature. The one-dimensional problem for the Gaussian curvature minimization problem over the finest grid is given as follows

$$\min_{c \in \mathbb{R}} |K(u(x) + c)| + \frac{\alpha}{2} (c - f^*(x))^2. \quad (16)$$

Similarly, we use the FBS scheme to solve the local problem (16). The only difference is how to estimate the minimizer of curvature regularization term. Supposing that ι tangent planes are enumerated, we can estimate ι normal curvatures κ_ℓ , $\ell = 1, 2, \dots, \iota$ in the local patch. According to differential geometry theory, the normal curvature can be calculated as

the quotient of *the second fundamental form* and *the first fundamental form* as follows

$$\kappa_\ell = \frac{II}{I} \approx \frac{d_\ell}{ds^2},$$

where d_ℓ denotes the distance of a neighboring point to the tangent plane and ds denotes the arclength between the neighboring point and the central point. Then Gaussian curvature can be defined by the two principal curvatures as

$$K(u_{k_1, k_2}) = \kappa_{\min} \kappa_{\max},$$

where the principal curvatures are obtained by $\kappa_{\min} = \min\{\kappa_\ell(u_{k_1, k_2})\}$, $\kappa_{\max} = \max\{\kappa_\ell(u_{k_1, k_2})\}$ for $\ell = 1, \dots, \ell$. We further denote $\kappa^*(u_{k_1, k_2}) = \min\{|\kappa_{\min}|, |\kappa_{\max}|\}$ be the principal curvature with the smaller absolute value, and T^* be the corresponding tangent plane. Thereupon, we have the following proposition to estimate the analytical solution for Gaussian curvature minimization.

Proposition 2. *The correction c on each point $(k_1, k_2) \in \Omega$ to minimize the Gaussian curvature $|K(u_{k_1, k_2} + c)|$ is given as $c^* = d^*$, where d^* is the distance of (k_1, k_2, u_{k_1, k_2}) to the tangent plane T^* .*

Proof. Since the point $(k_1, k_2, u_{k_1, k_2} + d^*)$ is on the tangent plane w.r.t. the principle curvature, we have $0 = |K(u_{k_1, k_2} + d^*)| \leq |K(u_{k_1, k_2})|$. \square

Then, we can use Algorithm 1 to solve the patch problem (16), and both the multi-grid method and domain decomposition method can be applied to solve the Gaussian curvature minimization problem (15) without much effort. Therefore, we omit the details here.

IV. NUMERICAL EXPERIMENTS

In this section, we evaluate the performance of the proposed multi-grid algorithm on image denoising problem. The qualities of the denoised images are measured by both the Peak Signal to Noise Ratio (PSNR) and the Structural Similarity Index Measure (SSIM). All of the experiments are implemented in a MATLAB R2016a environment on a desktop with an Intel Core i5 CPU at 3.3 GHz and 8 GB memory.

A. The effect of the multi-grid method

The choice of the maximal number of layers is important in the proposed multi-grid method, which affects the numerical performance of the curvature minimizations. We implement both multi-grid mean curvature (MGMC) and multi-grid Gaussian curvature (MGGC) methods on test images shown in Fig. 5, which are corrupted by white Gaussian noise with zero mean and standard deviation $\sigma = 10$. In the experiment, the regularization parameter varies as $\alpha = \{0.1, 0.06, 0.03\}$ and the number of layers changes as $J = \{1, 2, 3, 4, 5, 6\}$. Both MGMC and MGGC are stopped when the following relative error of the numerical energy is smaller than the predefined tolerance

$$RelErr(F(u^{t+1})) = |F(u^{t+1}) - F(u^t)|/F(u^{t+1}) \leq \epsilon, \quad (17)$$

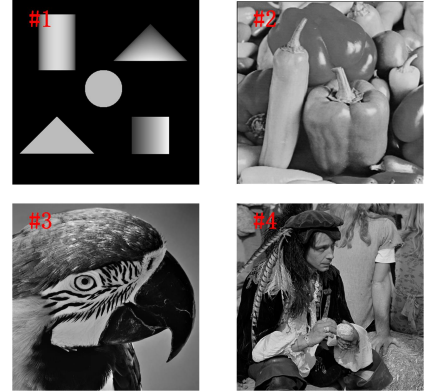


Fig. 5. The test images used in the numerical experiments, where the image ‘Triangle’ and ‘Peppers’ are of size 512×512 , image ‘Parrot’ and ‘Man’ are of size 1024×1024 .

which is set as $\epsilon = 10^{-6}$. For local minimization problem, we set the number of inner iteration for Algorithm 1 as 15 and its initial step size as $\eta^0 = 1$.

Table I displays the number of iterations, CPU time, and numerical energies for different combinations of the number of grid layers J and regularization parameter α . As can be seen, both MGMC and MGGC converge to similar numerical energies for a fixed value of α . Besides, we also conclude the following two observations

- Introducing the coarse layers can greatly reduce the outer iterations. Much CPU time is saved by increasing the maximum layers from $J = 1$ to $J = 3$. However, the CPU time increases as J keeps increases to $J = 6$ for all examples.
- The advantage of the multi-grid method is dominant when the regularization parameter α becomes smaller and smaller. The computational time of the single layer method is almost doubled as α grows from $\alpha = 0.1$ to $\alpha = 0.03$, while the growth of the multi-grid method is much smaller.

Thus, we set the number of layers is fixed as $J = 3$ for both MC and GC models in the following experiments.

B. Complexity discussion

We verify the linear convergence of our multi-grid method on both image ‘Triangle’ and ‘Parrot’, the size of which vary as $\{128 \times 128, 256 \times 256, 512 \times 512, 1024 \times 1024, 2048 \times 2048\}$. All images are corrupted by Gaussian noises with zero mean and standard deviation $\sigma = 10$. We set the regularization parameter as $\alpha = 0.06$ and the error tolerance as $\epsilon = 10^{-7}$. We implement both V-cycle (fine-to-coarse-to-fine) and half V-cycle (fine-to-coarse). The comparison results of the number of iterations, PSNR, CPU(s), and CPU ratio are recorded in Table II. By CPU ratio, it can be checked that the computational time of both V-cycle and half of V-cycle is proportional to the size of image N , and of complexity $\mathcal{O}(N)$. For different sizes of images, the half of V-cycle algorithm always consumes fewer costs than the V-cycle one, especially for images of size 2048×2048 down by a sixth, without sacrificing any accuracy. Therefore, the fine-to-coarse structure is used in our experiments.

TABLE I
THE DENOISING RESULTS ON TEST IMAGES TO DIFFERENT NUMBERS OF LAYERS FOR THE NOISE LEVEL $\sigma = 10$.

	α	Mean curvature						Gaussian curvature											
		0.1			0.06			0.03			0.1			0.06			0.03		
J	Iter	CPU(s)	Energy	Iter	CPU(s)	Energy	Iter	CPU(s)	Energy	Iter	CPU(s)	Energy	Iter	CPU(s)	Energy	Iter	CPU(s)	Energy	
#1	1	257	24.41	2.3158	378	38.01	2.4117	417	34.41	2.5074	118	10.05	1.8541	197	15.47	2.1098	275	21.10	2.3178
	2	77	8.96	2.3004	80	9.43	2.4161	114	13.21	2.5077	32	4.84	1.8496	41	4.81	2.1064	40	6.72	2.2934
	3	55	5.39	2.2835	62	5.47	2.4003	67	8.67	2.5071	27	3.66	1.8465	35	4.07	2.1002	43	5.82	2.2911
	4	57	8.74	2.2821	65	8.98	2.4005	77	10.94	2.5078	31	4.84	1.8471	30	4.80	2.1005	43	5.92	2.2972
	5	61	10.11	2.2891	61	6.65	2.4008	68	9.42	2.5077	31	4.68	1.8496	37	5.70	2.1005	41	6.26	2.2936
	6	56	9.84	2.2875	60	7.91	2.4009	69	9.67	2.5072	30	4.80	1.8496	32	4.92	2.1006	37	5.68	2.2914
#2	1	195	21.28	2.2833	318	32.16	2.4764	431	43.97	2.4703	120	10.43	1.8855	188	15.46	2.1717	254	20.82	2.3629
	2	80	9.23	2.2675	93	11.65	2.4754	107	12.91	2.4772	53	6.69	1.8776	73	9.33	2.1529	86	10.81	2.3661
	3	56	7.56	2.2637	64	9.37	2.4557	95	13.64	2.4721	47	6.65	1.8641	59	8.14	2.1512	76	10.46	2.3635
	4	50	7.98	2.2639	66	10.54	2.4558	106	15.81	2.4722	46	6.88	1.8691	65	9.81	2.1513	71	10.45	2.3625
	5	52	8.03	2.2641	60	9.91	2.4595	98	14.45	2.4761	46	6.95	1.8639	56	9.21	2.1517	69	10.13	2.3617
	6	60	10.45	2.2641	64	10.75	2.4536	106	16.61	2.4737	50	7.56	1.8684	56	9.86	2.1514	69	10.21	2.3642
#3	1	159	58.76	1.1672	227	85.18	1.3693	293	100.2	1.5325	124	46.99	8.7315	184	68.37	1.1333	246	90.40	1.3789
	2	42	23.66	1.1512	54	32.49	1.3647	54	29.81	1.5339	46	25.92	8.7362	57	30.69	1.1205	63	35.93	1.3769
	3	38	23.24	1.1512	51	26.86	1.3646	59	28.71	1.5155	44	27.30	8.7352	50	31.58	1.1064	54	33.96	1.3536
	4	41	26.67	1.1529	43	29.01	1.3661	47	31.78	1.5174	45	23.91	8.7358	58	38.63	1.1094	84	57.77	1.3529
	5	40	27.75	1.1522	42	29.35	1.3671	49	31.77	1.5220	44	29.23	8.7353	56	38.10	1.1028	73	51.80	1.3560
	6	42	29.72	1.1548	42	27.87	1.3667	51	33.67	1.5202	44	29.56	8.7358	52	35.79	1.1038	77	54.39	1.3592
#4	1	177	65.96	1.2591	273	98.02	1.5321	350	124.4	1.7344	127	47.95	9.4909	186	69.20	1.2658	245	89.48	1.3643
	2	54	25.59	1.2585	57	30.33	1.5366	59	30.44	1.7259	53	31.34	9.4814	60	36.25	1.2664	73	40.80	1.3463
	3	43	26.36	1.2588	50	26.68	1.5371	53	29.32	1.7233	49	31.75	9.4709	56	34.67	1.2615	60	37.00	1.3406
	4	38	24.23	1.2523	41	28.46	1.5327	57	30.74	1.7234	47	33.21	9.4702	55	35.73	1.2618	73	49.36	1.3412
	5	45	28.58	1.2599	45	28.69	1.5364	51	32.33	1.7237	41	32.50	9.4716	52	35.68	1.2616	52	45.34	1.3415
	6	47	30.81	1.2602	47	29.99	1.5323	43	31.45	1.7239	49	35.07	9.4724	54	38.92	1.2615	50	44.06	1.3411

TABLE II
THE COMPARED RESULT OF THE NUMBER OF ITERATIONS, PSNR, CPU(S), AND CPU RATIO FOR DIFFERENT SIZE IMAGES WITH V-CYCLE AND HALF OF THE V-CYCLE (DENOTED BY H-V-CYCLE).

Method	Sizes	N	#1				#3			
			#	PSNR	CPU	CPU Ratio	#	PSNR	CPU	CPU Ratio
H-V-cycle	128	16384	85	32.63	0.72	—	78	22.93	0.84	—
	256	65536	65	35.19	2.27	3.2	61	25.43	2.01	2.4
	512	262144	65	38.91	9.14	4.0	57	28.23	8.21	4.0
	1024	1048576	63	40.65	36.94	4.0	48	32.85	30.34	3.8
	2048	4194304	62	41.19	148.50	4.0	47	34.15	122.45	4.0
V-cycle	128	16384	63	32.66	1.01	—	64	22.94	0.98	—
	256	65536	63	35.12	2.83	2.8	58	25.42	2.68	2.7
	512	262144	62	38.91	11.82	4.0	55	28.18	10.25	4.0
	1024	1048576	60	40.68	44.01	4.0	47	32.85	38.31	3.8
	2048	4194304	59	41.19	179.75	4.0	45	34.15	152.68	4.0

C. Comparison with curvature filters

In what follows, we verify the advantages of the proposed multi-grid method by comparing it with multi-grid method in [12] and curvature filter [33]. Note that the domain decomposition method has been applied to the curvature filter for a fair comparison. We degrade the test images in Fig. 5 by the white Gaussian noises with zero mean and standard deviation $\sigma = 10$. The regularization parameter α are set as $\alpha = \{0.1 \ 0.06 \ 0.03\}$ and error tolerance is fixed as $\epsilon = 10^{-6}$ for all methods. There is no other parameters for mean curvature filter (CFMC) and Gaussian curvature filter (CFGc), where both methods are solved by gradient flow as presented in [33]. The parameters of multi-grid method [12] (denoted by MG) are set as: the total number of iteration is 10, the maximal level is 3, the stopping condition is set as (17), and all other parameters are set as suggested by the paper.

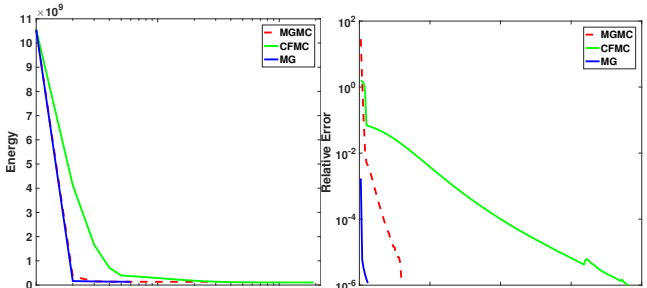
Table III records the PSNR, the number of iterations, CPU time, and the numerical energies obtained by different approaches. As can be seen, our method always achieves higher PSNR and smaller energies than curvature filter, while provides better or similar PSNR as the MG method. More importantly, much CPU time can be saved by our fine-to-coarse strategy, especially for the images of large scales and regularization parameters. We notice that multi-grid method [12] is very time consuming for solving the high-order PDEs. Obviously, our multi-grid method can well balance the efficiency and effectiveness. Both decays of the numerical energy and relative error of numerical energy for image ‘Parrot’ are plotted in Fig. 6, which demonstrate the fast convergence of our multi-grid approach.

More than that, we evaluate and compare the performance of the multi-grid method and curvature filter on images corrupted

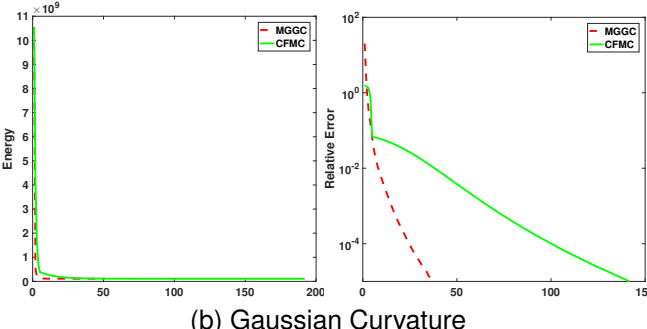
TABLE III

THE COMPARISON OF IMAGE DENOISING BETWEEN THE MULTI-GRID METHOD AND MEAN CURVATURE FILTER FOR THE NOISE LEVEL $\sigma = 10$.

Curvature		Mean curvature									Gaussian curvature					
	Im	$\alpha=0.1$			$\alpha=0.06$			$\alpha=0.03$			$\alpha=0.1$		$\alpha=0.06$		$\alpha=0.03$	
		CFMC	MG	MGMC	CFMC	MG	MGMC	CFMC	MG	MGMC	CFG	MGGC	CFG	MGGC	CFG	MGGC
PSNR	#1	40.43	41.81	42.24	40.88	42.83	43.01	40.82	42.61	42.58	38.15	39.84	39.01	41.61	38.96	41.09
	#2	33.54	35.42	35.49	33.67	35.57	35.61	33.24	35.39	35.52	33.67	35.64	33.87	35.85	33.19	35.41
	#3	30.19	32.17	32.23	30.21	32.84	32.85	29.67	32.12	32.24	30.52	32.91	31.89	33.92	30.44	31.83
	#4	30.17	32.51	32.42	30.26	32.62	32.68	29.46	31.37	32.25	29.49	31.66	29.84	32.23	29.41	30.44
Iter	#1	118	6	55	214	8	62	346	8	67	154	45	253	55	363	73
	#2	125	7	56	220	8	64	325	8	95	114	47	268	59	335	76
	#3	134	5	38	199	6	51	362	6	59	124	44	191	50	351	54
	#4	135	6	43	208	8	50	382	8	53	124	49	186	56	350	60
CPU(s)	#1	9.21	110.25	5.39	10.15	124.31	5.47	17.21	148.01	8.67	9.31	3.66	13.25	4.07	20.13	5.82
	#2	10.24	116.07	7.56	13.21	125.48	9.37	19.62	130.24	13.64	9.12	6.65	14.13	8.14	16.12	10.46
	#3	27.15	475.21	23.24	45.15	482.68	26.86	51.64	499.21	28.71	34.41	27.30	47.41	30.58	80.46	33.96
	#4	28.32	463.93	26.36	50.87	550.68	28.68	60.85	562.41	29.32	41.12	31.75	55.14	34.67	67.12	37.00
Energy	#1	2.4556	2.2946	2.2838	2.4871	2.4087	2.4003	2.5577	2.4982	2.5071	1.9186	1.8465	2.1904	2.1009	2.3539	2.2811
	#2	2.3478	2.2746	2.2639	2.5609	2.4615	2.4557	2.5502	2.4821	2.4721	1.9261	1.8641	2.2485	2.1510	2.5352	2.3635
	#3	1.2409	1.1588	1.1512	1.4527	1.3698	1.3646	1.6183	1.5213	1.5155	8.8509	8.7352	1.2284	1.1064	1.4294	1.3536
	#4	1.3415	1.2598	1.2588	1.6692	1.5435	1.5371	1.8582	1.7998	1.7259	9.5501	9.4709	1.3216	1.2615	1.4164	1.3406



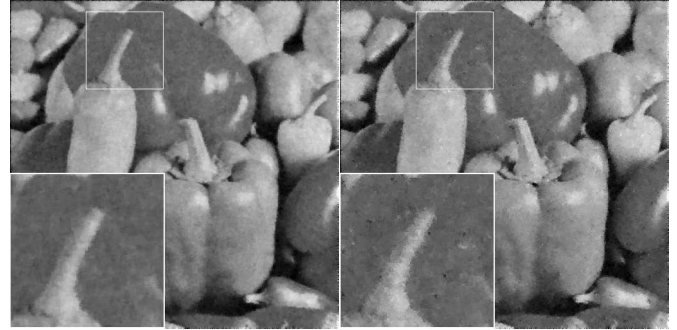
(a) Mean Curvature



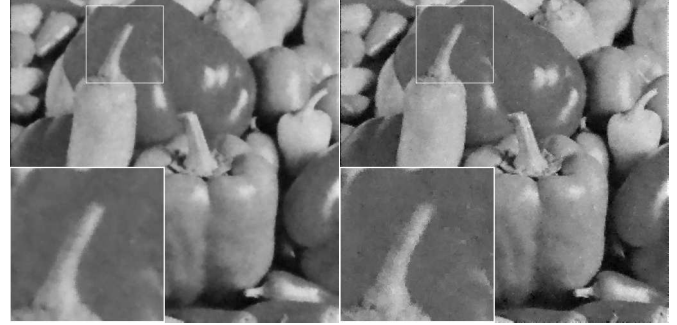
(b) Gaussian Curvature

Fig. 6. The decays of the numerical energy and relative error for both MC and GC methods on image 'Parrot' with the noise level $\sigma = 10$ and $\alpha = 0.06$.

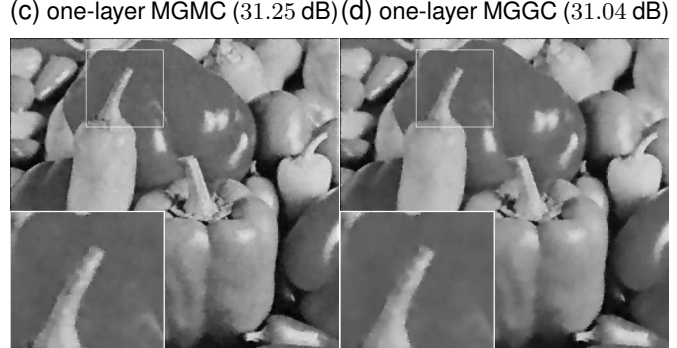
by different noise levels, i.e., $\sigma = \{10, 20, 30\}$, where α is chosen to achieve best restoration results. As provided in Table IV, our multi-grid method always outperforms the curvature filter in both image quality and computational efficiency. The main reason behind is that both mean curvature and Gaussian curvature in our model are estimated by the definitions in differential geometry. To make it more clearly, we present one representative restoration results in Fig. 7, where the results of the one-layer multi-grid methods are also illustrated for comparison. It can be observed the one-layer multi-grid methods produce much better results than curvature filters with much smoother details. And the multi-grid strategy can further improve the restoration quality.



(a) CFMC (29.75 dB)



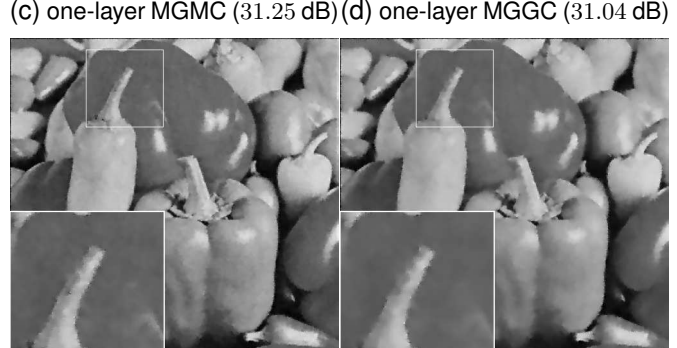
(b) CFGC (29.89 dB)



(c) one-layer MGMC (31.25 dB)



(d) one-layer MGGC (31.04 dB)



(e) MGMC (31.51 dB)



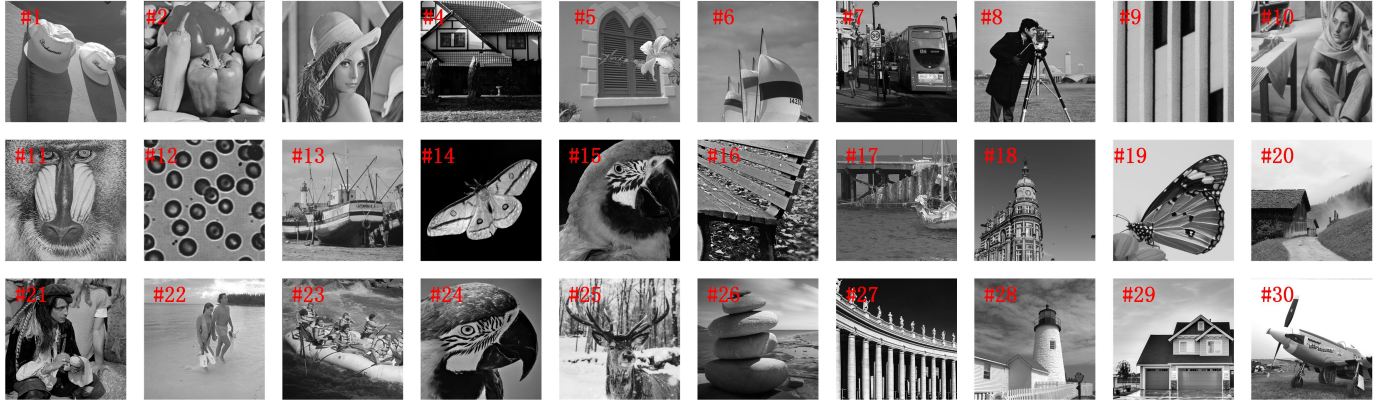
(f) MGGC (31.33 dB)

Fig. 7. The denoised results obtained by curvature filter and our method on image 'Pepper' with noise level $\sigma = 30$.

TABLE IV

THE COMPARISON BETWEEN THE MULTI-GRID METHOD AND CURVATURE FILTER WITH DIFFERENT NOISE LEVELS OF $\sigma = 10, 20, 30$, RESPECTIVELY.

	α	$\sigma = 10, \alpha = 0.06$		$\sigma = 20, \alpha = 0.05$		$\sigma = 30, \alpha = 0.04$		$\sigma = 10, \alpha = 0.06$		$\sigma = 20, \alpha = 0.05$		$\sigma = 30, \alpha = 0.03$	
		CFMC	MGMG	CFMC	MGMG	CFMC	MGMG	CFG	MGGC	CFG	MGGC	CFG	MGGC
PSNR	#1	40.88	43.01	35.17	38.11	33.87	35.53	39.01	41.61	34.51	37.33	32.31	35.19
	#2	33.67	35.61	30.95	33.37	29.75	31.51	33.87	35.85	31.09	33.52	29.89	31.33
	#3	30.21	32.85	28.22	30.48	26.94	29.11	31.89	33.92	27.97	29.61	26.21	28.14
	#4	30.26	32.68	27.39	29.51	26.28	28.35	29.84	32.23	27.18	28.55	25.62	27.22
CPU(s)	#1	10.15	5.47	13.11	5.88	21.41	6.42	13.25	4.07	18.95	6.88	34.45	7.29
	#2	13.21	9.37	15.41	10.34	24.47	14.78	14.13	8.14	19.25	11.17	37.76	10.47
	#3	45.15	26.86	67.97	26.42	72.13	33.85	47.41	30.58	79.94	30.23	82.72	39.37
	#4	50.87	28.68	70.98	29.42	78.67	35.11	55.14	34.67	97.42	36.41	98.42	40.45
Energy	#1	2.4871	2.4003	8.2315	8.1815	2.0181	2.0104	2.1904	2.1009	8.3539	8.2546	1.9741	1.9387
	#2	2.5609	2.4557	8.5179	8.3194	2.0155	1.9791	2.2485	2.1575	8.4884	8.3789	1.9833	1.9257
	#3	1.4527	1.3646	3.8236	3.6539	7.1025	6.9583	1.2284	1.1064	3.8313	3.7934	8.5485	8.3979
	#4	1.6692	1.5371	3.9651	3.7614	6.8714	6.6511	1.3216	1.2615	3.9682	3.9344	8.7079	8.6038

Fig. 8. The denoising dataset includes 30 gray images, where the size of images #1 – #15 is 512×512 and the size of images #16 – #30 is 1024×1024 .

D. Comparison with state-of-the-art variational methods

In this subsection, we compare our mean curvature method with several state-of-the-art image denoising methods on a dataset containing 30 gray images as shown in Fig. 8, where all images are degraded by white Gaussian noise of zero mean and standard deviation $\sigma = 20$. All methods are terminated by the relative error in u as given below

$$RelErr(u^{t+1}) = |u^{t+1} - u^t|/u^{t+1} < \epsilon, \quad (18)$$

where ϵ is fixed as $\epsilon = 10^{-4}$. The parameters of the comparison methods are provided as follows

- 1) ROF model [34]: The step sizes of primal dual method are set as $\tau = 1/(8\sigma)$ and $\sigma = 1/4$ for the primal and dual variable.
- 2) CFMC [33]: The regularization parameter is set as $\alpha = 0.05$.
- 3) Euler's elastica model (denoted as Euler) [8]: The parameters of ALM are fixed as $a = 1, b = 10, \mu = 10, \eta = 200, r_1 = 2, r_2 = 200, r_4 = 250$.
- 4) Mean curvature model (denoted as MC) [11]: The parameters of ALM are set as $\varepsilon = 0.4, \lambda = 1600, r_1 = 200, r_2 = 200, r_3 = 1 \times 10^4$ and $r_4 = 1 \times 10^4$.
- 5) Total absolute mean curvature model (denoted as TAC) [16]: The model is solved by the ADMM-based algorithm with the parameters given by $a = 1, b = 0.4, \lambda = 0.09$, and $r = 2$.

- 6) MGMG: The regulation parameter is set as $\alpha = 0.05$. The iteration number for solving the sub-problem $J(c)$ is fixed as 15.

Table V records both PSNR and SSIM obtained by different approaches, where our method gives the best restoration qualities. As we expected, the curvature methods give better results than the ROF model except for curvature filter. The reason behind is that we use more neighboring points to estimate the update for the central point, see the examples in Fig. 9.

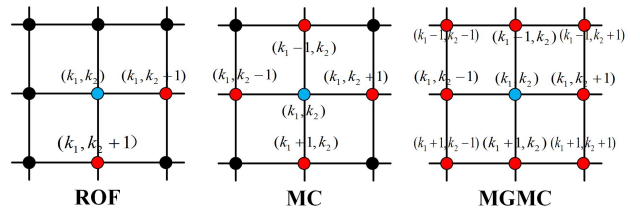


Fig. 9. The illustration of points used to estimate the update for the central point (blue one), where the red points are used for calculation.

Fig. 10 displays the CPU time of different methods, where the left plot contains images numbered from #1 to #15 with size of 512×512 and the right plot contains images numbered from #16 to #30 with size of 1024×1024 . It can be observed, among the curvature minimization approaches, our method is the fastest one followed by CFMC, TAC, Euler's elastica and MC model. Furthermore, both MC and Euler's elastica

TABLE V

THE COMPARISON OF SSIM AND PSNR (DB) AMONG THE ROF, CFMC, EULER'S ELASTICA, TOTAL ABSOLUTE MEAN CURVATURE, MEAN CURVATURE AND OUR MULTI-GRID MEAN CURVATURE MODEL ON 30 TEST IMAGES.

	SSIM						PSNR					
	ROF	CFMC	Euler	MC	TAC	MGMC	ROF	CFMC	Euler	MC	TAC	MGMC
#1	0.8458	0.8362	0.8548	0.8618	0.8652	0.8678	32.71	30.94	32.85	33.05	33.12	33.23
#2	0.8813	0.8348	0.8928	0.9115	0.9066	0.9124	31.55	30.00	31.77	31.85	31.97	32.32
#3	0.9256	0.8758	0.9355	0.9391	0.9311	0.9393	30.17	28.81	30.33	30.70	30.55	30.80
#4	0.8841	0.7225	0.9092	0.9183	0.9156	0.9192	25.76	24.01	25.98	26.44	26.16	26.75
#5	0.8957	0.7652	0.9011	0.9142	0.9118	0.9169	32.17	31.35	32.32	32.61	32.54	32.81
#6	0.8211	0.8142	0.8315	0.8323	0.8311	0.8410	31.18	30.27	31.32	31.42	31.51	31.66
#7	0.8391	0.7634	0.8483	0.8491	0.8489	0.8496	27.64	25.71	27.93	28.22	28.09	28.24
#8	0.7592	0.7019	0.7665	0.7787	0.7793	0.7798	30.91	28.54	31.13	31.37	31.29	31.42
#9	0.7685	0.6365	0.7747	0.7945	0.7981	0.7981	28.08	27.78	28.28	28.48	28.63	28.63
#10	0.8938	0.8008	0.9042	0.9095	0.9007	0.9098	30.75	29.37	30.98	31.38	31.37	31.71
#11	0.8473	0.7369	0.8501	0.8521	0.8514	0.8572	24.56	23.30	24.73	24.68	24.72	24.75
#12	0.8603	0.8381	0.8655	0.8764	0.8741	0.8791	32.10	30.04	32.32	32.74	32.73	32.97
#13	0.8119	0.7536	0.8151	0.8194	0.8233	0.8235	28.48	27.18	28.73	29.08	28.84	29.16
#14	0.8735	0.7269	0.8824	0.8855	0.8838	0.8875	32.09	29.54	32.12	32.37	32.24	32.36
#15	0.6786	0.5914	0.7207	0.7311	0.7321	0.7324	28.37	27.45	28.67	28.81	28.88	29.08
AVG	0.8391	0.7599	0.8502	0.8582	0.8569	0.8609	29.77	28.29	29.96	30.21	30.18	30.39
#16	0.8504	0.7695	0.8539	0.8624	0.8622	0.8642	28.61	26.17	28.79	28.90	28.95	29.22
#17	0.8208	0.8138	0.8307	0.8315	0.8308	0.8401	30.92	29.82	31.05	31.22	31.14	31.28
#18	0.7387	0.7107	0.7408	0.7413	0.7352	0.7421	32.86	29.48	33.01	33.35	33.28	33.38
#19	0.8893	0.7969	0.8942	0.9087	0.8931	0.9091	32.31	30.04	32.88	33.28	33.21	33.30
#20	0.8065	0.7513	0.8329	0.8362	0.8389	0.8392	29.24	28.16	29.39	29.55	29.59	29.63
#21	0.8150	0.7070	0.8268	0.8312	0.8280	0.8325	28.75	27.88	28.81	29.54	29.53	29.62
#22	0.8772	0.7073	0.8794	0.8807	0.8803	0.8834	27.39	26.92	27.45	27.66	27.73	27.88
#23	0.8813	0.8025	0.8835	0.8841	0.8852	0.8859	29.50	27.55	29.60	29.67	29.67	29.74
#24	0.9164	0.8577	0.9248	0.9402	0.9439	0.9476	30.04	28.61	30.21	30.59	30.52	30.68
#25	0.7775	0.6943	0.7861	0.7976	0.7965	0.7985	29.18	28.75	30.04	30.42	30.65	30.81
#26	0.8338	0.8023	0.8459	0.8449	0.8466	0.8468	33.82	32.88	34.01	34.28	34.21	34.33
#27	0.7302	0.6926	0.7451	0.7468	0.7489	0.7491	27.02	25.62	27.23	27.43	27.46	27.49
#28	0.9294	0.8595	0.9397	0.9401	0.9387	0.9402	26.56	25.51	26.71	26.93	26.86	26.88
#29	0.8257	0.7464	0.8296	0.8371	0.8369	0.8376	31.76	30.94	32.88	32.99	32.86	32.99
#30	0.8124	0.7696	0.8159	0.8241	0.8238	0.8254	32.51	31.20	33.69	33.82	33.71	33.89
AVG	0.8336	0.7588	0.8420	0.8471	0.8459	0.8494	30.03	28.50	30.38	30.64	30.62	30.74

model spend similar computational time, more than TAC, which is in accord with our complexity analysis. Similar to previous experiments, our MGMC not only gives much better restoration results, also saves half of CPU time.

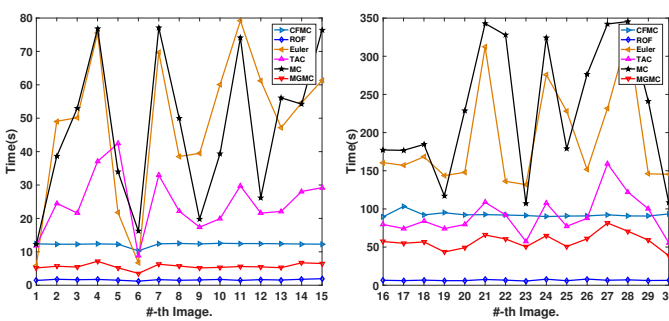


Fig. 10. The computational time comparison among different methods on the 30 test images.

Besides, we display the restoration results on image #15 and #21 corrupted by the noise level $\sigma = 20$ in Fig. 11. The restorations obtained by the ROF model exhibit the staircase effect, while the curvature regularization models give much smoother details. More importantly, by observing the results of image #15, our proposed method can preserve very good textural structures, while other methods have smoothed out the fine details. In summary, we conclude that our multi-grid method achieves the best performance on image restoration

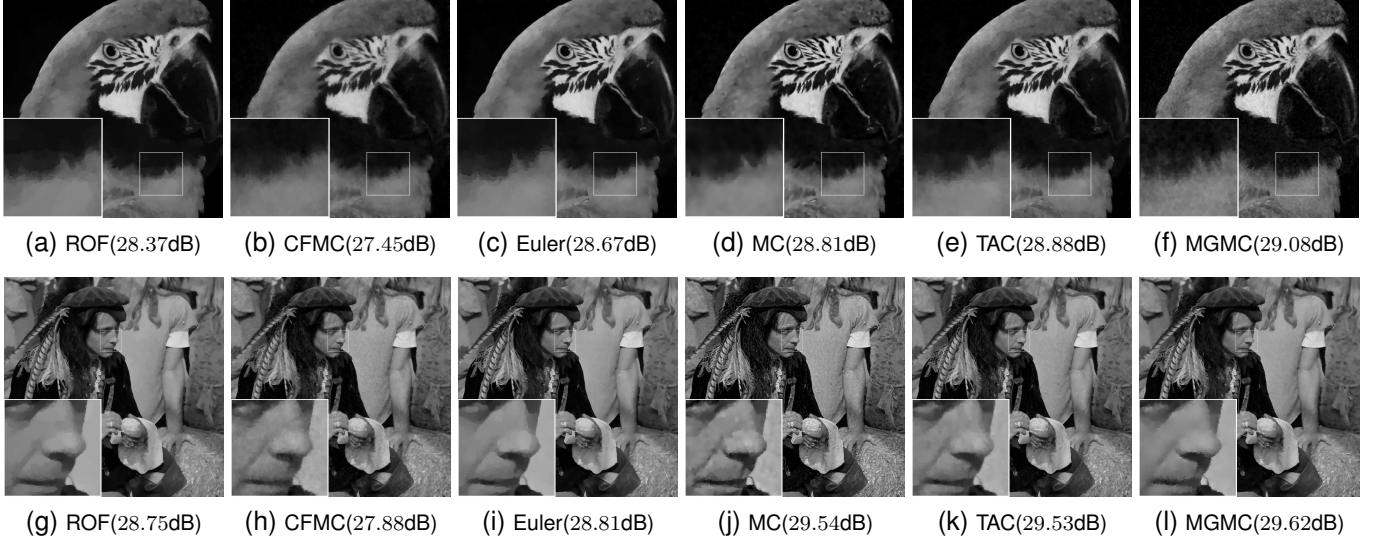
problem with high efficiency, which dose not trade the accuracy for speed.

V. APPLICATION TO CT RECONSTRUCTION

In this section, we extend the curvature regularization method and multi-grid strategy to more general inverse problems. The X-ray computed tomography (CT) has been widely used in medical diagnosis and industrial nondestructive testing, which aims to recover u from the observed data defined by

$$b = Au + \nu, \quad (19)$$

with ν being the random noise and A being the Radon transform. The CT reconstruction algorithms can be roughly divided into two categories [35]: the analytic algorithms and the iterative algorithms. The latter is known to be able to provide better reconstruction images especially when the inverse problem (19) becomes ill-posed [36]. The total variation regularization [25], TV stokes model [37] and total generalized variation (TGV) [38], [39] have been studied as the regularization and was shown effective for sparse CT reconstruction problems. The curvature regularization has also been used for image reconstruction problems [40], [41], which are shown effective in recovering the missing details and preserving geometric information. Besides, the multi-grid method has also been applied for CT reconstruction to achieve better reconstruction results [25], [42].

Fig. 11. The denoised results obtained by different methods on image #15 and #21 with noise level of $\sigma = 20$.

A. Mean curvature regularization for CT reconstruction

We use the mean curvature as the regularization term and concern with the following sparse CT reconstruction problem

$$\min_u \frac{1}{2} \|Au - b\|_2^2 + \alpha \sum_{x \in \Omega} |H(u(x))|, \quad (20)$$

which is solved by the aforementioned multi-grid method. Similarly, we implement the non-overlapping domain decomposition method on each layer to make the subproblems become independent and can be solved in parallel. The sub-minimization problems belonging to the same color are gathered as follows

$$\min_{c_j \in \mathbb{R}^{N_k}} \frac{1}{2} \|A(u + \sum_{i \in I_k} c_j^i \phi_j^i) - b\|_2^2 + \alpha \sum_{i \in I_k} \sum_{x \in \tau_j^i} |H(u(x) + c_j^i \phi_j^i(x))|.$$

According to Proposition 1, the above subproblem can be further reformulated into the following quadratic problem

$$\min_{c_j \in \mathbb{R}^{N_k}} \frac{1}{2} \|A(u + \sum_{i \in I_k} c_j^i \phi_j^i) - b\|_2^2 + \alpha \sum_{i \in I_k} (c_j^i - d_j^i)^2, \quad (21)$$

where the closed-form solution is given as

$$\begin{bmatrix} L_{1,1} & \cdots & \langle A\phi_j^1, A\phi_j^{N_k} \rangle \\ \langle A\phi_j^2, A\phi_j^1 \rangle & \cdots & \langle A\phi_j^2, A\phi_j^{N_k} \rangle \\ \vdots & \vdots & \vdots \\ \langle A\phi_j^{N_k-1}, A\phi_j^1 \rangle & \cdots & \langle A\phi_j^{N_k-1}, A\phi_j^{N_k} \rangle \\ \langle A\phi_j^{N_k}, A\phi_j^1 \rangle & \cdots & L_{N_k, N_k} \end{bmatrix} \begin{bmatrix} c_j^1 \\ c_j^2 \\ \vdots \\ c_j^{N_k-1} \\ c_j^{N_k} \end{bmatrix} = \begin{bmatrix} r_j^1 \\ r_j^2 \\ \vdots \\ r_j^{N_k-1} \\ r_j^{N_k} \end{bmatrix} \quad (22)$$

with

$$L_{i,i} = \langle A\phi_j^i, A\phi_j^i \rangle + 2\alpha, \quad \text{and} \quad r_j^i = \langle b - Au, A\phi_j^i \rangle + 2\alpha d_j^i,$$

for $i = 1, \dots, N_k$. For such a symmetric linear system, we can implement the conjugate gradient as the numerical solver.

B. Numerical examples

Now we discuss the numerical examples of the proposed multi-grid algorithm for CT reconstruction problem. Two phantom images ‘Shepp-Logan’ and ‘Forbild-gen’ with the size of 512×512 and 1024×1024 , are used to evaluate the performance. We adopt the parallel-beam geometry for both images in the experiments and set the projection numbers to be $N_p = 18$ and 36 .

In what follows, we evaluate the effectiveness and efficiency of the proposed multi-grid method by comparing it with the total variation model [25], which is also implemented by the multi-grid method. The implementation details are described as follows

- 1) The multi-grid total variation model (denoted by MGT) [25]: The parameters are set as $\alpha = 3.5 \times 10^{-5}$ and 2×10^{-5} for projection number $N_p = 18$ and 36 , respectively, and $\beta = 10^{-6}$ for noiseless experiments. We set $\alpha = 3 \times 10^{-4}$ and 5×10^{-4} for $N_p = 18$ and 36 on the noise level $\sigma = 0.005$.
- 2) The multi-grid mean curvature model (denoted by MGMC): The parameters are set as $\alpha = 4 \times 10^{-3}$ and 3×10^{-3} for projection number $N_p = 18$ and 36 , respectively. We set $\alpha = 1 \times 10^{-4}$ and 2×10^{-4} for $N_p = 18$ and 36 on the noise level $\sigma = 0.005$.

Both multi-grid methods are stopped using the relative error of the numerical energy (17) for $\epsilon = 10^{-4}$ and the stopping criteria for the linear system (22) is when the iteration number reaches the maximum iteration number of 10. The number of layers are set as $J = 4$ for both algorithms.

The comparison results of PSNR, SSIM, CPU time, the number of iterations and CPU time per iteration are all recorded in Table VI. For different combinations of images and projection numbers, our MGMC always gives higher PSNR and SSIM than MGT, which benefits from the strong priors of the curvature regularization. In terms of computational efficiency, because our local minimization problem has the analytical solution, the computational efficiency of our MGMC

TABLE VI

THE PSNR, SSIM, CPU TIME, THE NUMBER OF ITERATIONS (DENOTED BY #) AND CPU TIME PER ITERATION (DENOTED BY CPU/I) FOR CT RECONSTRUCTION WITH PROJECTION NUMBERS OF $N_p = 18$ AND 36, WHERE IMAGE INTENSITY IS PROJECTED TO $[0, 1]$.

Sizes		512 ($\sigma = 0$)		1024 ($\sigma = 0$)		512 ($\sigma = 0.005$)		1024 ($\sigma = 0.005$)	
Examples		Shepp-Logan	Fobild-gen	Shepp-Logan	Fobild-gen	Shepp-Logan	Fobild-gen	Shepp-Logan	Fobild-gen
18	MGMCM GTV	MGMCM GTV	MGMCM GTV	MGMCM GTV	MGMCM GTV	MGMCM GTV	MGMCM GTV	MGMCM GTV	MGMCM GTV
	PSNR	36.85 34.08	33.01 31.38	32.42 30.88	28.52 27.18	29.37 28.52	24.67 24.18	29.37 28.99	24.48 23.57
	SSIM	0.9901 0.9881	0.9801 0.9746	0.9044 0.8947	0.8574 0.8361	0.8846 0.8508	0.8579 0.7126	0.8949 0.8735	0.8818 0.8715
	CPU	68.65 51.72	79.05 68.74	287.61 300.24	350.64 480.24	57.19 60.52	65.27 80.36	325.45 394.28	380.48 452.51
36	#	104 89	124 112	134 127	134 126	114 96	130 120	121 105	132 125
	CPU/I	0.4782 0.3612	0.474 0.4647	0.4769 2.1793	2.6016 3.6585	0.5016 0.6304	0.5021 0.6696	2.6896 3.7551	2.8824 3.4041
	PSNR	44.66 43.18	38.81 37.8	39.24 38.35	37.24 36.15	33.09 31.85	28.22 26.78	31.72 29.18	28.97 26.17
	SSIM	0.9962 0.9911	0.993 0.991	0.9914 0.9899	0.9854 0.9749	0.8796 0.8506	0.8579 0.8391	0.9245 0.9024	0.8546 0.8355
	CPU	90.65 73.23	98.85 77.23	376.43 454.75	486.42 654.75	80.54 90.23	89.85 110.25	345.52 425.45	454.46 500.58
	#	116 108	134 128	145 139	168 151	128 125	151 142	138 131	152 148
	CPU/I	0.6197 0.5188	0.594 0.4916	2.4745 3.1462	2.7804 4.2162	0.6291 0.7218	0.5956 0.7764	2.5037 3.2477	2.9767 3.3822

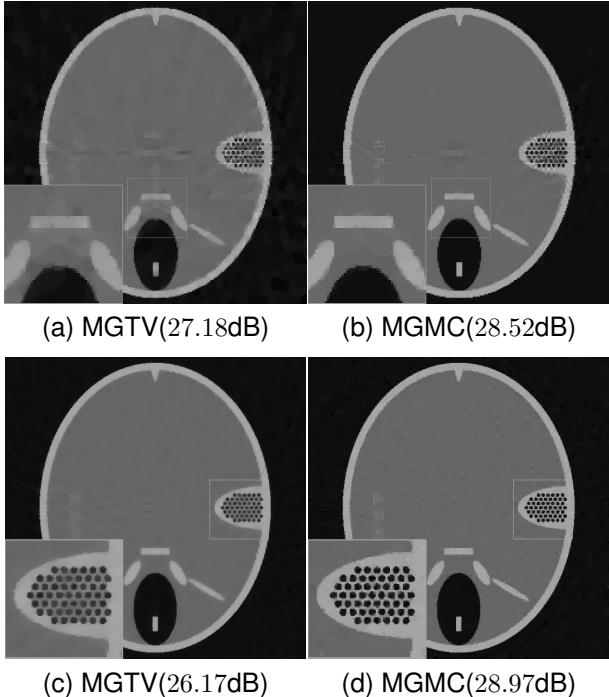


Fig. 12. The comparison results on 'Forbild-gen' with size of 1024×1024 and projection numbers be $N_p = 18$, while the second row is the result with noise level 0.005 and the projection numbers be $N_p = 36$.

is quite high, which is verified by the CPU time per iteration. On the other hand, it requires to solve a nonlinear PDE on the local problems for TV regularization model, which is time consuming. The advantages of our method becomes stronger for the large-scale problems that our curvature regularization model performs faster than TV model. Finally, we present the selective reconstruction results in Fig. 12. As can be seen, our MGMC outperforms the MGTB method, which produces homogeneous results with fine details and small structures.

VI. CONCLUSION

We proposed an efficient multi-grid algorithm for solving the curvature-based minimization problem that relies on the piecewise constant basic spanned subspace correction. The original minimization is then transferred into series of local problems from the fine layer to coarse layer, each of which was

solved by the forward-backward splitting scheme with convergence guarantee. More importantly, there exists the analytical solutions to the sub-minimization problems on local patches, which make the local problems can be solved very efficiently. Furthermore, we applied the non-overlapping domain decomposition method on each layer to increase the parallelism for improving the computational efficiency. Comparative experiments on image denoising and reconstruction problems demonstrate the efficacious and efficient performance of the proposed method by comparing it with several advanced denoising methods. Our future work includes developing more efficient algorithms for curvature-related minimization models and expand the applications of curvature regularization, e.g., improving the robustness of deep neural network models [43]–[45].

APPENDIX PROOF OF LEMMA 1

Proof. Followed Lemma 1 in [32], the first-order optimality condition of c^{t+1} gives

$$c^{t+1} = c^t + (\eta^t)^2 c^{t+\frac{1}{2}} - \eta^t \nabla r(c^{t+1}). \quad (23)$$

The convexity of $r(c)$ implies that for any \tilde{c}

$$r(\tilde{c}) \geq r(c^{t+1}) + \langle \nabla r(c^{t+1}), \tilde{c} - c^{t+1} \rangle. \quad (24)$$

By expanding the squared norm of the difference between c^{t+1} and \tilde{c} , it gives

$$\begin{aligned} \|c^{t+1} - \tilde{c}\|^2 &= \|c^t - \tilde{c}\|^2 + (\eta^t)^2 \|c^{t+\frac{1}{2}} - \nabla r(c^{t+1})\|^2 \\ &\quad - 2\eta^t \langle \nabla r(c^{t+1}) - \eta^t c^{t+\frac{1}{2}}, c^{t+1} - \tilde{c} \rangle \\ &\quad - 2\eta^t \langle \nabla r(c^{t+1}) - \eta^t c^{t+\frac{1}{2}}, c^{t+1} - c^t \rangle. \end{aligned}$$

We now use (23) and (24) to get

$$\begin{aligned} \|c^{t+1} - \tilde{c}\|^2 &\leq \|c^t - \tilde{c}\|^2 - 2\eta^t r(c^{t+1}) \\ &\quad + 2\eta^t r(\tilde{c}) + 2(\eta^t)^2 G + 2(\eta^t)^2 D, \end{aligned} \quad (25)$$

By Proposition 1, we have

$$|H(u^t + c^{t+\frac{1}{2}})| \leq |H(u^t + \tilde{c})|. \quad (26)$$

Sum (25) and (26), we obtain

$$\begin{aligned} 2\eta^t (|H(u^t + c^{t+\frac{1}{2}})| + r(c^{t+1}) - J(\tilde{c})) &\leq \|c^t - \tilde{c}\|^2 \\ &\quad - \|c^{t+1} - \tilde{c}\|^2 + 2(\eta^t)^2 (G + D), \end{aligned}$$

which completes the proof. \square

REFERENCES

- [1] A. Belyaev and P.-A. Fayolle, "Adaptive curvature-guided image filtering for structure+ texture image decomposition," *IEEE Transactions on Image Processing*, vol. 27, no. 10, pp. 5192–5203, 2018.
- [2] H. Pei, B. Wei, K. Chang, C. Zhang, and B. Yang, "Curvature regularization to prevent distortion in graph embedding," *Advances in Neural Information Processing Systems*, vol. 33, pp. 20779–20790, 2020.
- [3] B. Dong, H. Ju, Y. Lu, and Z. Shi, "Cure: Curvature regularization for missing data recovery," *SIAM Journal on Imaging Sciences*, vol. 13, no. 4, pp. 2169–2188, 2020.
- [4] L. I. Rudin, S. Osher, and E. Fatemi, "Nonlinear total variation based noise removal algorithms," *Physica D: Nonlinear Phenomena*, vol. 60, no. 4, pp. 259–268, 1992.
- [5] Y. Meyer, "Oscillating patterns in image processing and nonlinear evolution equations," *University Lecture Ser.* 22, AMS, 2002.
- [6] M. Lysaker, A. Lundervold, and X.-C. Tai, "Noise removal using fourth-order partial differential equation with applications to medical magnetic resonance images in space and time," *IEEE Transactions on Image Processing*, vol. 12, no. 12, pp. 1579–1590, 2003.
- [7] K. Bredies, K. Kunisch, and T. Pock, "Total generalized variation," *SIAM Journal on Imaging Sciences*, vol. 3, no. 3, pp. 492–526, 2010.
- [8] X. C. Tai, J. Hahn, and G. J. Chung, "A fast algorithm for Euler's Elastica model using augmented lagrangian method," *SIAM Journal on Imaging Sciences*, vol. 4, no. 1, pp. 313–344, 2011.
- [9] W. Zhu and T. Chan, "Image denoising using mean curvature of image surface," *SIAM Journal on Imaging Sciences*, vol. 5, no. 1, pp. 1–32, 2012.
- [10] A. Chambolle and T. Pock, "Total roto-translational variation," *Numerische Mathematik*, no. 1, 2018.
- [11] W. Zhu, X. C. Tai, and T. Chan, "Augmented lagrangian method for a mean curvature based image denoising model," *Inverse Problems and Imaging*, vol. 7, no. 4, pp. 1409–1432, 2017.
- [12] C. Brito-Loeza and K. Chen, "Multigrid algorithm for high order denoising," *SIAM Journal on Imaging Sciences*, vol. 3, no. 3, pp. 363–389, 2010.
- [13] L. Alboul and R. Damme, "Polyhedral metrics in surface reconstruction: Tight triangulations," *The Mathematics of Surfaces*, pp. 309–336, 1997.
- [14] M. Elsey and S. Esedoglu, "Analogue of the total variation denoising model in the context of geometry processing," *SIAM Journal on Multiscale Modeling and Simulation*, vol. 7, no. 4, pp. 1549–1573, 2009.
- [15] C. Brito-Loeza, K. Chen, and V. Uc-Cetina, "Image denoising using the gaussian curvature of the image surface," *Numerical Methods for Partial Differential Equations*, vol. 32, no. 3, pp. 518–527, 2015.
- [16] Q. Zhong, K. Yin, and Y. Duan, "Image reconstruction by minimizing curvatures on image surface," *Journal of Mathematical Imaging and Vision*, vol. 63, no. 1, pp. 30–55, 2021.
- [17] Y. Gong and I. F. Sbalzarini, "Curvature filters efficiently reduce certain variational energies," *IEEE Transactions on Image Processing*, vol. 26, no. 4, pp. 1786–1798, 2017.
- [18] Nash and Stephen, "A multigrid approach to discretized optimization problems," *Optimization Methods and Software*, vol. 14, no. 1, pp. 99–116, 2000.
- [19] R. Kimmel and I. Yavneh, "An algebraic multigrid approach for image analysis," *SIAM Journal on Scientific Computing*, vol. 24, no. 4, pp. 1218–1231, 2003.
- [20] C. Frohn-Schauf, S. Henn, and K. Witsch, "Nonlinear multigrid methods for total variation image denoising," *Computing and Visualization in Science*, vol. 7, no. 4, pp. 199–206, 2004.
- [21] T. F. Chan and K. Chen, "On a nonlinear multigrid algorithm with primal relaxation for the image total variation minimisation," *Numerical Algorithms*, vol. 41, no. 4, pp. 387–411, 2006.
- [22] K. Chen and X. C. Tai, "A nonlinear multigrid method for total variation minimization from image restoration," *Journal of Scientific Computing*, vol. 33, no. 2, pp. 115–138, 2007.
- [23] J. Savage and K. Chen, "An improved and accelerated non-linear multigrid method for Total-Variation denoising," *International Journal of Computer Mathematics*, vol. 82, no. 8, pp. 1001–1015, 2005.
- [24] T. F. Chan and K. Chen, "An optimization based multilevel algorithm for total variation image denoising," *Multiscale Modeling and Simulation*, vol. 5, no. 2, pp. 615–645, 2006.
- [25] Z. Zhang, X. Li, Y. Duan, K. Yin, and X.-C. Tai, "An efficient multi-grid method for TV minimization problems," *Inverse Problems and Imaging*, vol. 15, no. 5, pp. 125–138, 2021.
- [26] X.-C. Tai, L.-J. Deng, and K. Yin, "A multigrid algorithm for maxflow and min-cut problems with applications to multiphase image segmentation," *Journal of Scientific Computing*, vol. 87, no. 3, pp. 101–128, 2021.
- [27] N. Chumchob, K. Chen, and C. Brito-Loeza, "A fourth-order variational image registration model and its fast multigrid algorithm," *SIAM Journal on Multiscale Modeling and Simulation*, vol. 9, no. 1, pp. 89–128, 2011.
- [28] P. L. Combettes and V. R. Wajs, "Signal recovery by proximal forward-backward splitting," *Multiscale Modeling and Simulation*, vol. 4, no. 4, pp. 1168–1200, 2005.
- [29] H. Raguet, J. Fadili, and G. Peyré, "A generalized forward-backward splitting," *SIAM Journal on Imaging Sciences*, vol. 6, no. 3, pp. 1199–1226, 2013.
- [30] N. Pustelnik, C. Chaux, and J.-C. Pesquet, "Parallel proximal algorithm for image restoration using hybrid regularization," *IEEE Transactions on Image Processing*, vol. 20, no. 9, pp. 2450–2462, 2011.
- [31] V. H. Tang, A. Bouzerdoum, and S. L. Phung, "Compressive radar imaging of stationary indoor targets with low-rank plus jointly sparse and total variation regularizations," *IEEE Transactions on Image Processing*, vol. 29, pp. 4598–4613, 2020.
- [32] J. Duchi and Y. Singer, "Efficient online and batch learning using forward backward splitting," *The Journal of Machine Learning Research*, vol. 10, pp. 2899–2934, 2009.
- [33] Y. Gong, "Mean curvature is a good regularization for image processing," *IEEE Transactions on Circuits and Systems for Video Technology*, vol. 29, no. 8, pp. 2205–2214, 2019.
- [34] A. Chambolle and T. Pock, "A first-order primal-dual algorithm for convex problems with applications to imaging," *Journal of Mathematical Imaging and Vision*, vol. 40, no. 1, pp. 120–145, 2010.
- [35] G. T. Herman, *Fundamentals of computerized tomography*. Fundamentals of Computerized Tomography, 2010.
- [36] J. Qi and R. M. Leahy, "Iterative reconstruction techniques in emission computed tomography," *Physics in Medicine and Biology*, vol. 51, no. 15, p. R541, 2006.
- [37] Y. Liu, Z. Liang, J. Ma, H. Lu, K. Wang, H. Zhang, and W. Moore, "Total variation-stokes strategy for sparse-view X-ray CT image reconstruction," *IEEE transactions on medical imaging*, vol. 33, no. 3, pp. 749–763, 2013.
- [38] S. Niu, Y. Gao, Z. Bian, J. Huang, W. Chen, G. Yu, Z. Liang, and J. Ma, "Sparse-view X-ray CT reconstruction via total generalized variation regularization," *Physics in Medicine and Biology*, vol. 59, no. 12, pp. 2997–3009, 2014.
- [39] J. Chen, L. Wang, B. Yan, H. Zhang, and G. Cheng, "Efficient and robust 3D CT image reconstruction based on total generalized variation regularization using the alternating direction method," *Journal of X-ray science and Technology*, vol. 23, no. 6, pp. 683–698, 2015.
- [40] H. Zhang, L. Wang, Y. Duan, L. Li, G. Hu, and B. Yan, "Euler's Elastica strategy for limited-angle computed tomography image reconstruction," *IEEE Transactions on Nuclear Science*, vol. 64, no. 8, pp. 2395–2405, 2017.
- [41] M. Yan and Y. Duan, "Nonlocal elastica model for sparse reconstruction," *Journal of Mathematical Imaging and Vision*, vol. 62, no. 4, pp. 532–548, 2020.
- [42] D. Marlevi, H. Kohr, J.-W. Buurlage, B. Gao, K. J. Batenburg, and M. Colarieti-Tosti, "Multigrid reconstruction in tomographic imaging," *IEEE Transactions on Radiation and Plasma Medical Sciences*, vol. 4, no. 3, pp. 300–310, May 2020.
- [43] S.-M. Moosavi-Dezfooli, A. Fawzi, J. Uesato, and P. Frossard, "Robustness via curvature regularization, and vice versa," in *Proceedings of the IEEE/CVF Conference on Computer Vision and Pattern Recognition (CVPR)*, June 2019, pp. 9070–9078.
- [44] Y. Guo, L. Chen, Y. Chen, and C. Zhang, "On connections between regularizations for improving dnn robustness," *IEEE Transactions On Pattern Analysis And Machine Intelligence*, vol. 43, no. 12, pp. 4469–4476, 2020.
- [45] V. Singla, S. Singla, S. Feizi, and D. Jacobs, "Low curvature activations reduce overfitting in adversarial training," in *Proceedings of the IEEE/CVF International Conference on Computer Vision (ICCV)*, October 2021, pp. 16423–16433.